Antiphase dynamics in a multimode semiconductor laser with optical injection

S. Osborne,[1] A. Amann,[1] K. Buckley,[1] G. Ryan,[1] S. P. Hegarty,[1] G. Huyet,[1,2] and S. O'Brien[1]
[1]*Tyndall National Institute, University College, Lee Maltings, Cork, Ireland*
[2]*Department of Applied Physics and Instrumentation, Cork Institute of Technology, Cork, Ireland*
(Received 2 December 2008; published 25 February 2009)

A detailed experimental study of antiphase dynamics in a two-mode semiconductor laser with optical injection is presented. The device is a specially designed Fabry-Pérot laser that supports two primary modes with a terahertz frequency spacing. Injection in one of the primary modes of the device leads to a rich variety of single and two-mode dynamical scenarios, which are reproduced with remarkable accuracy by a four-dimensional rate equation model. Numerical bifurcation analysis reveals the importance of torus bifurcations in mediating transitions to antiphase dynamics and of saddle node of limit-cycle bifurcations in switching of the dynamics between single- and two-mode regimes.

DOI: 10.1103/PhysRevA.79.023834 PACS number(s): 42.55.Px, 42.65.Sf, 05.45.−a

I. INTRODUCTION

The semiconductor laser with optical injection is a conceptually simple system that nevertheless has complex nonlinear dynamical properties. Phenomena of interest that have been observed experimentally include subharmonic resonance [1], period-doubling route to chaos [2,3], and bistability of wave mixing and injection locked states [4,5]. Use of numerical continuation tools has enabled diverse dynamical states of the single-mode edge-emitting system with optical injection to be linked together in a consistent way [6]. More recently, a global picture of the complex dynamics of polarization modes in vertical cavity surface emitting lasers (VCSELs) with orthogonal optical injection has also begun to emerge [7].

For both fundamental and applied reasons, interest in multimode dynamics of semiconductor lasers has increased. This follows from their increased dynamical complexity, as well as possible applications in optical signal processing [8,9]. Multiple oscillating modes allow for antiphase behavior, where mutual coupling of individual modal degrees of freedom leads to anticorrelated intensity dynamics [10–14].

Recently, we have developed a specially engineered two-mode diode laser with a large (terahertz) primary mode spacing [15]. The device can be biased such that it oscillates on two modes simultaneously with the same average power level. Unlike the case of polarization modes in VCSELs, the mode spacing is in the highly nondegenerate regime, allowing us to develop studies of the multimode nonlinear dynamics in the minimal possible two-mode system. These studies provide a means to test models of the multimode diode laser and to reveal new bifurcation structure that occurs beyond the single-mode approximation [16].

A number of approaches have been developed to modeling the multimode dynamics of edge-emitting semiconductor lasers. Partial differential equations will generally reproduce experimental results, but such an approach suffers from computational difficulty and the reduced level of physical insight provided [17,18]. Rate equation approaches have proven very successful in the case of modeling the dynamical response of single-mode semiconductor lasers. In the case of multimode dynamics, however, a number of different models have been developed that differ in how the dynamics of the carrier density are described [14,19–21].

Here we provide an experimental and theoretical study of antiphase dynamics when one of the two primary modes of the device is optically injected. Among the rich variety of multimode dynamical phenomena we have found limit cycle, quasiperiodic and chaotic antiphase dynamics, as well as regions where the optical power is largely switched to the *uninjected* mode. As we will show, all of these dynamics, as well as the familiar injection locking on a single mode, can be found by performing a sweep over a large detuning range of the injected field for a certain fixed injected field intensity. As the central theme of this study, we provide a detailed description of regions of quasiperiodic antiphase dynamics using spectrally resolved power spectral measurements and intensity time traces. We then demonstrate that a four-dimensional rate equation model reproduces the overall experimental picture very well. In particular, we show how regions of quasiperiodic antiphase dynamics that we have observed experimentally are reproduced in numerical simulations and that new bifurcation structure, which is particular to the two-mode system considered, governs the appearance of these dynamics.

This paper is organized as follows. In Sec. II, we describe our device and experimental setup and we provide optical and power spectral data that illustrate the variety of dynamical scenarios that can be observed as a function of frequency detuning at a fixed injected field strength. We also provide intensity time traces and power spectral data characterizing two regions of quasiperiodic antiphase dynamics. In Sec. III, we introduce our model equations that describe the two-mode injected system, showing how the overall experimental picture as well as specific examples of antiphase dynamics is qualitatively reproduced. Finally, in Sec. IV, we describe the bifurcation structure that leads to the antiphase dynamics observed.

II. EXPERIMENT

For the primary mode spacing of four fundamental Fabry-Pérot (FP) modes (480 GHz), we observe simultaneous lasing of the two primary modes. We adjust the device current

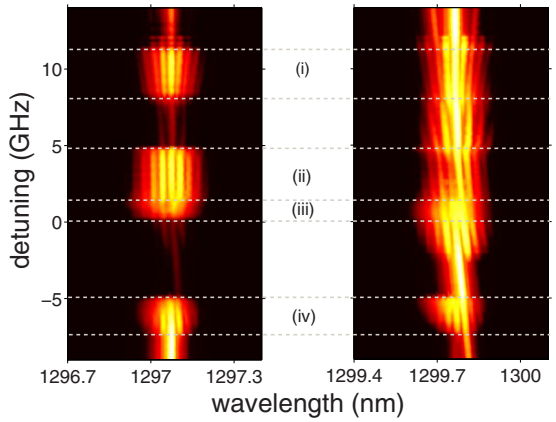

FIG. 1. (Color online) Optical spectra of the two-color device as the frequency detuning $\Delta\omega$ is varied at a fixed injection. Left: uninjected mode ν_1. Right: injected mode ν_2.

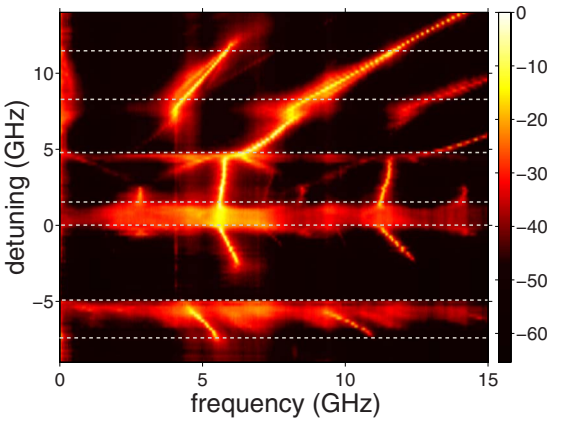

FIG. 2. (Color online) Power spectral density of the total intensity as a function of frequency detuning. The injected power level is the same as in Fig. 1

in order that the time-averaged optical power in each primary mode of the free-running laser is equal. Details of the design and free-running lasing characteristics of the device we consider can be found in Ref [15].

For our experiment, we use the two-color laser in a master-slave configuration, where the master laser is a tunable laser with <100 kHz linewidth. Choosing a fixed injected power level, we vary the detuning, $\Delta\omega$, of the injected field from the long-wavelength mode of the device, ν_2. The optical spectra of the two primary modes are shown as a function of the frequency detuning of the injected signal in Fig. 1 for a detuning range of -9 GHz$<\Delta\omega<14$ GHz. Despite the fact that we vary only the frequency detuning, Fig. 1 indicates that we are dealing with a rich dynamical scenario; regions of multiwavelength dynamics are interspersed with regions of single or nearly single-mode dynamics, where the optical power can be concentrated in either of the primary modes. In Secs. III and IV we will show that a minimal extension of the single-mode rate equation model by a single dynamical variable is sufficient to account for the presence of the uninjected mode and reproduces the experimental data with remarkable accuracy.

For this injected power level the power spectral density of the total intensity is plotted in Fig. 2. By considering the spectrum of the total intensity we naturally exclude the antiphase frequency components that are present in each region of two-mode dynamics. From Figs. 1 and 2, the regions of stable and unstable injection locking where the uninjected mode is off can be identified near zero detuning. In the injection locking region, a sharp single peak at the frequency of the injected field is present in the optical spectrum at long wavelength. In the region of unstable locking, which extends from approximately zero detuning to -2.5 GHz, a single frequency that is associated with undamped relaxation oscillations is visible in Fig. 2. This frequency is almost constant at c. 5.5 GHz, which we identify as the relaxation oscillation frequency of the device.

At large positive frequency detuning of 14 GHz, we find a broad region of nearly single-mode dynamics, where the optical power is concentrated in the injected mode. In this region the injected field and two weaker symmetrically placed components can be clearly resolved in the optical spectrum at long wavelength. Examining Fig. 2, we find that in the corresponding region only the detuning frequency is present. This is then a region of wave mixing or beating between the injected field and the long-wavelength primary mode.

As the detuning is decreased, a period-doubling bifurcation occurs and we enter a region where a new frequency equal to one half of the detuning frequency is present in Fig. 2. As indicated in Fig. 1, within this broad region we find region (i) of two-mode dynamics, where the optical spectra of both modes are considerably broadened. A representative set of power spectral densities and time traces of the total intensity and the individual modal intensities in region (i) is shown in Fig. 3. In this figure the detuning is 10 GHz. As expected the power spectrum of the total intensity shown in Fig. 3(b) comprises two broadened peaks which include distinctive shoulders.

In the power spectra of the intensities of the individual modes shown in Figs. 3(d) and 3(f) we can see a strong antiphase frequency component with a distinct peak at c. 400 MHz. We see also that the features associated with the injection frequency and its subharmonic in each of these figures are broadened further because of the formation of satellites due to mixing with the low-frequency antiphase component. Note also that the detuning of the injected signal is the dominant frequency in the dynamics of the injected mode [Fig. 3(f)] but the subharmonic near the relaxation oscillation frequency dominates in the dynamics of the uninjected mode [Fig. 3(d)].

We have confirmed that the low antiphase frequency is an independent frequency component that is not a linear combination of the other frequencies present. The low frequency is clearly visible as an envelope modulation of the intensity in the time traces of the individual modes shown in Figs. 3(c) and 3(e). These antiphase time traces have a distinctive sawtooth structure that results from the growing or decaying oscillations that form each pulse. They are remarkably similar to the so-called regular pulse packages that can be observed in semiconductor lasers with optical feedback in the short external cavity regime [22]. However, in the case of optical injection, the fast time scale is determined by the

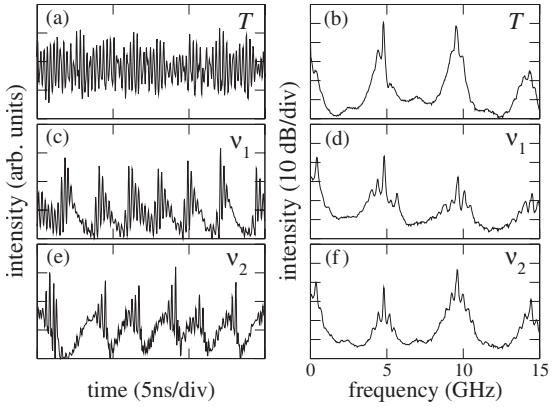

FIG. 3. Experimentally measured antiphase dynamics, region (i). The frequency detuning is 10 GHz and the injected power level is the same as in Fig. 1. Left panels: Intensity time traces. Right panels: Power spectral densities. [(a) and (b)] total intensity. [(c) and (d)] uninjected mode. [(e) and (f)] injected mode.

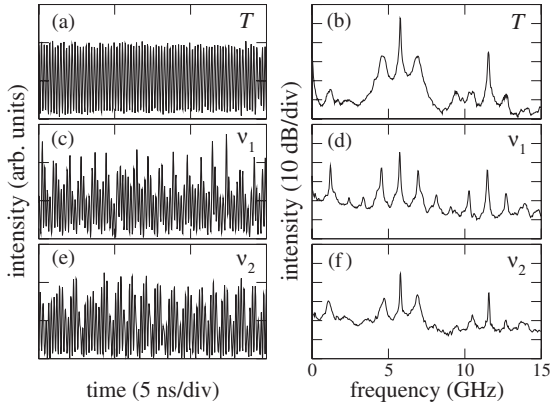

FIG. 4. Experimentally measured antiphase dynamics, region (ii). The frequency detuning is 4 GHz and the injected power level is the same as in Fig. 1. Left panels: Intensity time traces. Right panels: Power spectral densities. [(a) and (b)] total intensity. [(c) and (d)] uninjected mode. [(e) and (f)] injected mode.

relaxation oscillation and its harmonics, rather than the external cavity frequency.

As the detuning is decreased further a reverse period doubling occurs and a simple single-mode wave-mixing region is found. Adjacent to this region, we next find a second broad region of two-mode dynamics, which has a lower boundary at zero detuning. For reasons that will become clear, we subdivide this region into two, and label the subregions as regions (ii) and (iii). Broadly speaking, region (ii) is found once the detuning is less than the relaxation oscillation frequency. Note that across the boundary between the single-mode wave-mixing region and region (ii), the power spectrum of the total intensity briefly becomes strongly broadened. Then, as the detuning is decreased further, the dynamics become simpler with the relaxation oscillation frequency, and its harmonics, largely determining the dynamics of the total intensity.

A representative set of power spectral densities and time traces in region (ii) from inside this boundary is shown in Fig. 4. The dynamics of the total intensity is now largely determined by the relaxation oscillation and its harmonic although weak and broadened satellite features are also visible [cf. Fig. 4(b)].

From Figs. 4(d) and 4(f), we see that the dynamics of the individual modes are determined by a series of frequencies. In particular, there is a strong low-frequency component present in the individual dynamics of both modes that is almost completely in antiphase. As was the case in region (i), this low-frequency component is responsible for the appearance of a cascade of frequencies that are centered at the relaxation oscillation peak and its harmonic.

As the detuning is decreased further, the frequency difference between the relaxation oscillation and the detuning approaches half of the relaxation oscillation frequency. In this region a weak period-two region of the total intensity is found. For detunings less than approximately one half the relaxation oscillation frequency we find coupled chaotic dynamics that are characterized by broad-band spectra.

For negative detunings, the single-mode locking region is found, which extends to a detuning of approximately −5 GHz. At the boundary of the stable locking region, inside of which there is no structure in the power spectrum, we find region (iv), where the spectrum is again strongly broadened. Decreasing the detuning further, the spectrum is almost structureless. Here, a weak feature at the detuning frequency can be seen. This corresponds to the transfer of the optical power to the uninjected mode.

III. MODELING OF THE DEVICE RESPONSE

We have adapted the well-known model of a single-mode laser [1,19] with optical injection to account for the presence of a second lasing mode. The system of equations in normalized units may be written as follows [16]:

$$\dot{E}_1 = \tfrac{1}{2}(1 + i\alpha)[g_1(2n + 1) - 1]E_1, \tag{1}$$

$$\dot{E}_2 = \left\{\tfrac{1}{2}(1 + i\alpha)[g_2(2n + 1) - 1] - i\Delta\omega\right\}E_2 + K, \tag{2}$$

$$T\dot{n} = P - n - (1 + 2n)\sum_m g_m|E_m|^2, \tag{3}$$

where the nonlinear modal gain is

$$g_m = g_m^{(0)}\left(1 + \epsilon\sum_n \beta_{mn}|E_n|^2\right)^{-1}. \tag{4}$$

Here E_1 and E_2 are the normalized complex electric field amplitudes of the modes and n is the normalized excess carrier density. The bifurcation parameters are the normalized injected field strength K and the angular frequency detuning $\Delta\omega$. Further parameters are the phase-amplitude coupling α, the product of the carrier lifetime and the cavity decay rate T, the normalized pump current P, and the linear modal gain $g_m^{(0)}$. In our numerical simulation we used the values α=2.6, T^{-1}=0.00125, P=0.5, (twice threshold), and $g_m^{(0)}$=1. Then the value of the relaxation oscillation frequency is $\omega_{RO} = \sqrt{2P/T} \sim 5.5$ GHz, in agreement with experiment. The cross and self-saturation are determined by $\epsilon\beta_{mn}$ and we use

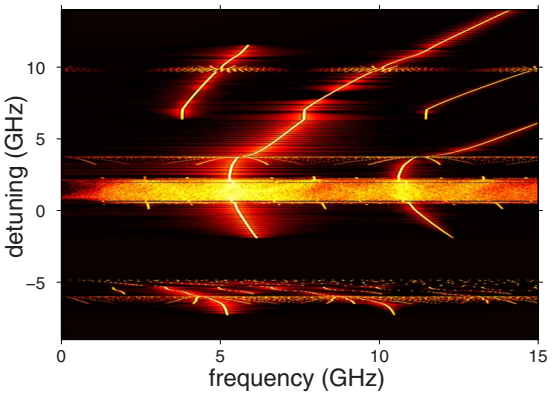

FIG. 5. (Color online) Power spectral density of the total field intensity $|E_1|^2+|E_2|^2$ obtained from numerical integration of Eqs. (1)–(3) as a function of the detuning. The injected field strength is $K=0.008$.

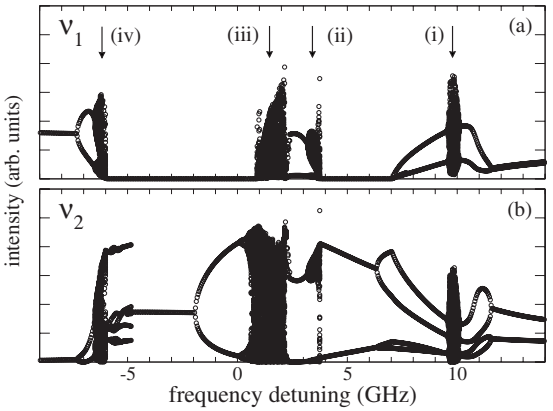

FIG. 6. Local extrema of the field intensities (a) $|E_1|^2$ and (b) $|E_2|^2$ obtained from numerical integration of Eqs. (1)–(3) as a function of the detuning. The injected field strength is $K=0.008$. Upper panel: uninjected field. Lower panel: injected field.

the values $\epsilon=0.01$, $\beta_{12}=\beta_{21}=2/3$, and $\beta_{11}=\beta_{22}=1$, which is consistent with the stability of the two-mode solution in the free-running laser.

Note that although we have provided a complex equation for the field E_1, the phase of E_1 is in fact decoupled, leading to a four-dimensional system of equations where only the intensity of the uninjected mode influences the dynamics. In addition, the single-mode dynamics is contained within the invariant submanifold ($E_1=0$) in these equations. Our model equations are therefore a minimal extension of the (three dimensional) single-mode case and follow from the fact that the primary mode spacing in the device considered is in the highly nondegenerate regime.

This system only considers a single-averaged carrier density and a general cross and self saturation of the gain. More complex models of the multiwavelength dynamics are available that are derived by considering additional Fourier components of the carrier density. One example includes the effect of static spatial hole burning explicitly leading to a system with two carrier density equations, one defined for each field [21]. However, we have found that these equations lead to some unphysical results in the injected system, such as a stable injection locked region where the uninjected mode is not suppressed.

Another modeling approach [14,23] includes an asymmetric term that is associated with a dynamic grating formed in the carrier density profile. This term effectively represents the mutual injection or wave-mixing interaction of the primary modes and has been shown to play a role in the *free-running* switching dynamics of Fabry-Pérot lasers [14]. This grating is also responsible for the formation of four-wave-mixing sidebands in the free-running two-mode laser considered here [15]. However, we have found equivalent experimental results for injection at both the long- and short-wavelength primary modes, suggesting that this grating does not significantly affect the dynamics. We attribute this to the very large separation of the primary modes of the device (480 GHz), which means that the dynamic grating is weakly developed, with large sidebands observed because of enhancement by the Fabry-Pérot cavity.

Using model Eqs. (1)–(3), in Fig. 5 we plot the power spectral density of the total field intensity $|E_1|^2+|E_2|^2$ for fixed K and for detuning $-9\ \text{GHz}<\Delta\omega<14\ \text{GHz}$. The value of K is 0.008 which was chosen as it provided the best possible agreement with experiment over the whole range of frequency detuning. When compared with the experimental result of Fig. 2, we find that the level of qualitative agreement is excellent.

To further illustrate that the individual modal dynamics are also well reproduced, in Fig. 6 we plot the local extrema of the numerically calculated field intensities, $|E_1|^2$ and $|E_2|^2$, over the same detuning range. If we examine the structure of Fig. 6, we can immediately identify two regions where the uninjected mode is off and that the position and extent of these regions is in good qualitative agreement with the experimental results shown in Fig. 1. Thus not only do the model equations reproduce the dynamics of the total intensity, they also provide an accurate picture of the regimes of single and multimode dynamics of the system. Note that this agreement extends to the model reproducing the strong suppression of the injected mode at large negative detunings that is observed experimentally.

In Fig. 6, vertical arrows indicate regions (i)–(iv) of two-mode dynamics that we have identified experimentally. For detailed comparison with experiment, we now provide the numerical intensity time traces and corresponding power spectra for the two regions of antiphase dynamics labeled (i) and (ii).

In Fig. 7, we show these data for the total intensity and for the intensities of each of the two modes at a detuning of 10.0 GHz, which is located in region (i). What is most striking is the reproduction of the sawtooth pulse package structure that was seen experimentally. The envelope period of the pulse packages is seen to be c. 300 MHz, in broad agreement with experiment. The cascade of equally spaced frequencies that begins at this envelope frequency is also almost completely in antiphase. The power spectrum of the total intensity is also seen to comprise two broad cascades formed by the envelope frequency, one centered at the detuning frequency and another at the relaxation oscillation frequency. However, the number of these peaks is much larger than was found experimentally in the case of the individual modes and, in fact, the

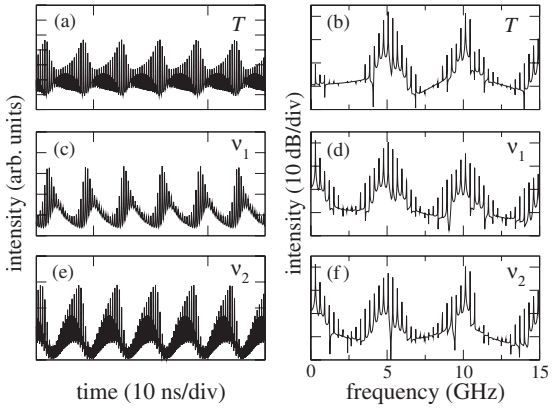

FIG. 7. Numerically computed antiphase dynamics, region (i). The frequency detuning is 10.0 GHz. The injected field strength is $K=0.008$. Left panels: Intensity time traces. Right panels: Power spectral densities. [(a) and (b)] total intensity. [(c) and (d)] uninjected mode. [(e) and (f)] injected mode.

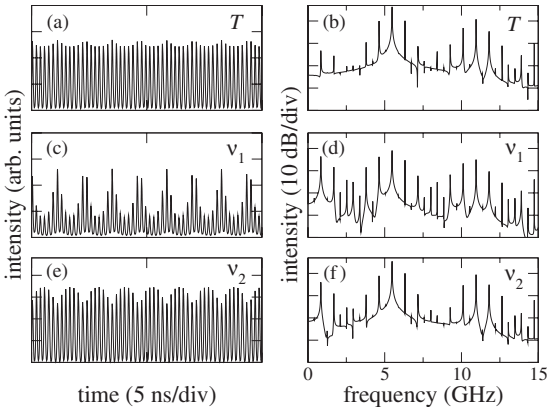

FIG. 8. Numerically computed antiphase dynamics, region (ii). The frequency detuning is 3.4 GHz. The injected field strength is $K=0.008$. Left panels: Intensity time traces. Right panels: Power spectral densities. [(a) and (b)] total intensity. [(c) and (d)] uninjected mode. [(e) and (f)] injected mode.

cascade structure that is seen in the numerical data for the total intensity is poorly resolved in the experiment.

In Fig. 8, we show these data for the total intensity and for the intensities of each of the two modes at a detuning of 3.4 GHz, which is located in region (ii). We have had to choose a slightly smaller value for the detuning frequency for this simulation because of the discrepancy that exists between the boundary of the central two-mode region that was found numerically and in the experiment. Nevertheless, the qualitative agreement with the experimental time traces and power spectra is again very good in this region. We note in particular the experimental intensity waveforms of the individual modes that are peaked in the case of the uninjected mode and rounded for the injected mode are well reproduced.

IV. BIFURCATION ANALYSIS

The bifurcations evident from Figs. 5 and 6 can be understood from the global bifurcation diagram in the $\Delta\omega$ vs K plane as shown in Fig. 9. Let us focus on the vertical line at injection strength $K=0.008$, which was used in Figs. 5 and 6 and identified to best fit the experimental data shown in Figs. 1 and 2. At large $\Delta\omega=15$ GHz we are in a two-mode wave-mixing region, with the uninjected mode ν_1 largely suppressed and weakly modulated. This agrees with the experimental observation of a weak but nonvanishing uninjected mode power in the region above region (i) in Fig. 1. As we lower the detuning frequency to $\Delta\omega\approx 12$ GHz, which is about twice the relaxation frequency ω_{RO}, the dynamical coupling between the uninjected mode and injected mode via the carrier density n [Eq. (3)] becomes relevant, and gives rise to a two-mode period-doubling bifurcation (magenta line in Fig. 9). This bifurcation line forms the upper boundary of the dynamical two-mode region (i), which we experimentally identified in Figs. 1 and 2.

As we further decrease $\Delta\omega$, we cut through a regime which is delineated by a torus bifurcation line (red line in Fig. 9) at $\Delta\omega\approx 10$ GHz. We emphasize that this torus bifurcation is a feature of the two-mode system that is not present in the single-mode case. Due to this torus bifurcation an additional incommensurate low frequency of about 300 MHz appears as previously identified in the discussion of the characteristic sawtooth antiphase time traces of Fig. 7. Note that outside of the boundary of the torus bifurcation, the two-mode period-doubled limit cycle is only weakly stable and noise will be able to excite low-frequency antiphase dynamics. This explains the relatively broad region of antiphase dynamics observed experimentally in Fig. 2. As we further lower the detuning frequency to $\Delta\omega\approx 7$ GHz, the two-mode limit cycle exchanges stability with a single-mode limit cycle in a transcritical bifurcation (striped blue line in Fig. 9). At this point the uninjected mode is completely switched off and the limit cycle in the single-mode manifold becomes stable, forming the lower boundary of the region (i). This scenario is in agreement with experimental data of Fig. 2, where we observe that the spectral density evolves continuously across the lower boundary of region (i).

As we decrease $\Delta\omega$ further, the single-mode period-doubled limit cycle undergoes an inverse period-doubling bifurcation (dashed magenta line in Fig. 9) and a single-period limit cycle is generated. This is experimentally verified by the disappearance of the frequency at $\Delta\omega\approx 4$ GHz, which happens below the lower boundary of region (i), i.e., *after* we have switched to a single-mode state.

The generated single-period limit cycle, which experimentally corresponds to the single-mode wave-mixing state, remains stable until we encounter a saddle-node bifurcation of limit cycles [orange line, saddle node of limit cycle (SNL) in Fig. 9] at $\Delta\omega\approx 4$ GHz. At this point the stable single-mode limit cycle collides with an unstable one, and both limit cycles disappear [25]. The dynamics are then blown out from the single-mode manifold where the associated bursting dynamics explains the brief broadening which is observed in the experimental spectrum (Fig. 2) and in the numerical spectrum (Fig. 5). Close to the bifurcation point, the remainder of the stable limit cycle still forms a slow region on the single-mode manifold, and thus the period of the resulting two-mode orbit diverges close to the bifurcation point. Away from the region of bursting dynamics this new incommensu-

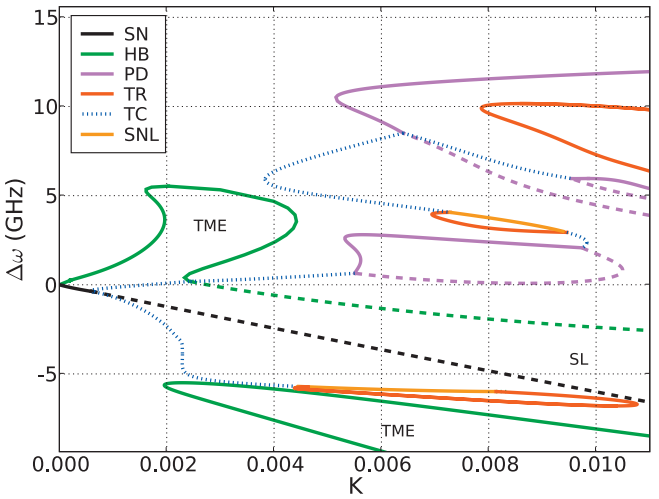

FIG. 9. (Color) Bifurcation diagram in the $\Delta\omega$ vs K plane of Eq. (1)–(3) calculated using the numerical continuation tool AUTO-07P [24]. Solid and dashed lines denote bifurcations of two-mode and single-mode states, respectively. The different types of bifurcations are indicated by SN (saddle node), HB (Hopf), PD (period doubling), SNL (saddle node of limit cycle), and TR (torus). The striped blue lines TC denote transcritical bifurcations between stable single-mode and stable two-mode states. The single-mode (stable) locking and two-mode equilibrium regions are denoted by SL and TME, respectively. Only bifurcation lines which affect stable states are shown.

rate frequency results in a quasiperiodic orbit on a torus (cf. Fig. 8).

Moving away from the SNL bifurcation point to lower $\Delta\omega$, the frequency originating at zero increases linearly, and gives rise to satellite peaks around the second major frequency close to the relaxation oscillation frequency. This explains the striking starlike features in the experimental (Fig. 2) and numerical (Fig. 5) spectra, which immediately follow the brief broadening discussed in the previous paragraph. Just below the SNL bifurcation, we are in a region with two incommensurate frequencies, which gives rise to quasiperiodic evolution on a stable torus manifold. The torus transforms into a limit cycle via an inverse torus bifurcation at $\Delta\omega \approx 3$ GHz (red line in Fig. 9), and in the power spectrum, the low frequency that was introduced by the SNL bifurcation disappears again.

Further lowering $\Delta\omega$ below 3 GHz we find that the stable two-mode limit cycle undergoes a period-doubling cascade to chaos. In Fig. 9 we only show the first period-doubling bifurcation (magenta line). At the transition to chaotic behavior the power spectrum broadens dramatically, which marks the transition from region (ii) to region (iii). We leave the chaotic regime at $\Delta\omega \approx 0$ in a single-mode periodic orbit, which undergoes inverse period-doubling bifurcations (dashed magenta line in Fig. 9).

As in basic single-mode laser theory, this limit cycle becomes a single-mode equilibrium locked state (SL) via a Hopf bifurcation (dashed green line in Fig. 9), which disappears in a saddle-node bifurcation (dashed black line in Fig. 9). Then the remaining single-mode limit cycle undergoes again a SNL bifurcation followed by a torus bifurcation, as was discussed in the context of region (ii). This defines the two-mode region (iv) of Fig. 1.

For even lower $\Delta\omega$ we find a two-mode equilibrium (TME) state, which is bounded by a Hopf bifurcation. This region corresponds to the experimentally observed region below region (iv) in Fig. 1, where the injected mode is suppressed. This suppression is a precursor to the appearance of a bistability between single-mode injection locking and a two-mode equilibrium at larger negative detunings (<-10 GHz) and larger values of the injected field strength. We have recently demonstrated that this bistability can be the basis of an all-optical memory element based on switching of the uninjected mode [16]. Interestingly, there is also a second two-mode equilibrium region for positive detuning and weak injection ($0<\Delta\omega<6$ GHz, $K<0.005$) as shown in Fig. 9. This region will be the subject of more detailed study in future work.

V. CONCLUSIONS

We have presented an experimental and theoretical study of antiphase dynamics in an optically injected two-mode laser diode. The device was a specially engineered Fabry-Pérot laser designed to support two primary modes with a large (terahertz) frequency spacing. At a fixed injected field strength, injection in one of the primary modes of the device leads to a rich dynamical scenario where dramatic switching between regions of two-mode and single-mode dynamics was observed as the frequency detuning was varied. Using a minimal extension of the single-mode rate equation model that includes a single equation for the carrier density and a general cross and self saturation of the gain, we reproduced experimental results with a high degree of accuracy. In particular, we were able to describe the dynamical sequence of the total intensity and of the individual modes. These dynamics were shown to be organized by complex bifurcation structure that results from the increased dimensionality of the two-mode injected system.

ACKNOWLEDGMENTS

This work was supported by Science Foundation Ireland and IRCSET. The authors thank Eblana Photonics for the preparation of sample devices and G. Bordyugov for helpful discussions.

[1] P. M. Varangis, A. Gavrielides, T. Erneux, V. Kovanis, and L. F. Lester, Phys. Rev. Lett. **78**, 2353 (1997).
[2] V. Kovanis, A. Gavrielides, T. B. Simpson, and J. M. Liu, Appl. Phys. Lett. **67**, 2780 (1995).
[3] I. Gatare, M. Sciamanna, J. Buesa, H. Thienpoint, and K. Panajotov, Appl. Phys. Lett. **88**, 101106 (2006).
[4] R. Hui, A. D'Ottavi, A. Mecozzi, and P. Spano, IEEE J. Quantum Electron. **27**, 1688 (1991).
[5] S. K. Hwang and J. M. Liu, Opt. Commun. **169**, 167 (1999).
[6] S. Wieczorek, B. Krauskopf, and D. Lenstra, Opt. Commun. **172**, 279 (1999).
[7] I. Gatare, M. Sciamanna, M. Nizette, and K. Panajotov, Phys. Rev. A **76**, 031803(R) (2007).
[8] L. Tsimring and M. M. Sushchik, Phys. Lett. A **213**, 155 (1996).
[9] M. Takenaka, M. Raburn, and Y. Nakano, IEEE Photonics Technol. Lett. **17**, 968 (2005).
[10] K. Wiesenfeld, C. Bracikowski, G. James, and R. Roy, Phys. Rev. Lett. **65**, 1749 (1990).
[11] P. Khandokhin, Y. Khanin, Y. Mamaev, N. Milovsky, E. Shirokov, S. Bielawski, D. Derozier, and P. Glorieux, Quantum Semiclassic. Opt. **10**, 97 (1998).
[12] M. A. Larotonda, A. M. Yacomotti, and O. E. Martinez, Opt. Commun. **169**, 149 (1999).
[13] A. Uchida, Y. Liu, I. Fischer, P. Davis, and T. Aida, Phys. Rev. A **64**, 023801 (2001).
[14] A. M. Yacomotti, L. Furfaro, X. Hachair, F. Pedaci, M. Giudici, J. Tredicce, J. Javaloyes, S. Balle, E. A. Viktorov, and P. Mandel, Phys. Rev. A **69**, 053816 (2004).
[15] S. O'Brien, S. Osborne, K. Buckley, R. Fehse, A. Amann, E. P. O'Reilly, L. P. Barry, P. Anandarajah, J. Patchell, and J. O'Gorman, Phys. Rev. A **74**, 063814 (2006).
[16] S. Osborne, K. Buckley, A. Amann, and S. O'Brien, e-print arXiv:0812.1900.
[17] J. K. White, J. V. Moloney, A. Gavrielides, V. Kovanis, A. Hohl, and R. Kalmus, IEEE J. Quantum Electron. **34**, 1469 (1998).
[18] G. Huyet, J. K. White, A. J. Kent, S. P. Hegarty, J. V. Moloney, and J. G. McInerney, Phys. Rev. A **60**, 1534 (1999).
[19] J. M. Buldú, F. Rogister, J. Trull, C. Serrat, M. C. Torrent, J. García-Ojalvo, and C. R. Mirasso, J. Opt. B: Quantum Semiclassical Opt. **4**, 415 (2002).
[20] C. Masoller, M. S. Torre, and P. Mandel, Phys. Rev. A **71**, 013818 (2005).
[21] I. V. Koryukin and P. Mandel, Phys. Rev. A **70**, 053819 (2004).
[22] T. Heil, I. Fischer, W. Elsäßer, and A. Gavrielides, Phys. Rev. Lett. **87**, 243901 (2001).
[23] P. Mandel, C. Etrich, and K. Otsuka, IEEE J. Quantum Electron. **29**, 836 (1993).
[24] E. J. Doedel, A. R. Champneys, T. Fairgrieve, Yu. Kuznetsov, B. Oldeman, R. Pfaffenroth, B. Sandstede, X. Wang, and C. Zhang, AUTO-07P, Continuation and bifurcation software for ordinary differential equations, Technical report, Concordia University Montreal, 2007 (http://indy.cs.concordia.ca/auto/).
[25] Y. A. Kuznetsov, *Elements of Applied Bifurcation Theory* (Springer, New York, 1995).